Research Letter

geodynamica

CPO2Hill: An Efficient Parametrisation to Infer Anisotropic Viscous Behaviour Directly from Olivine Texture Parameters

Ágnes Király *[1,2], **Yijun Wang** [2,3], **Clinton P. Conrad** [2], **Lars N. Hansen** [4], **Ben Mather** [5]

[1] *NJORD Centre, University of Oslo, Oslo, Norway*
[2] *Centre for Planetary Habitability, Department of Geosciences, University of Oslo, Oslo, Norway*
[3] *GFZ Helmholtz Centre for Geosciences, Potsdam, Germanyy*
[4] *Department of Earth and Environmental Sciences, University of Minnesota, Minneapolis, MN, USA*
[5] *School of Geography, Earth and Atmospheric Sciences, University of Melbourne, VIC, Australia*

Abstract

Anisotropic viscosity is likely prevalent within the upper mantle, but is usually disregarded in geodynamic models. At the crystal scale, olivine's intrinsic properties are such that dislocation creep occurs over an order of magnitude more easily along olivine's [100](001) and [100](010) slip systems than along its [001](010) slip system. However, deforming olivine aggregates generate crystallographic preferred orientations (CPO) with their own macroscopically effective anisotropic viscosities that have proven difficult to estimate from the microscopic anisotropies of individual olivine crystals. Here, we present CPO2Hill, a simple method to derive anisotropic viscosity parameters directly from the CPO's second-order mean orientation tensor. To calibrate the method, we created a large database of textures likely to occur in geodynamic simulations. We tested our method within numerical simulations of simple shear with both constant and varying shear directions and against laboratory experimental data. Finally, we integrated our method into the open-source geodynamic code ASPECT, where it can be used to explore the geodynamic importance of anisotropic viscosity.

Editor(s):
Lukas Fuchs
Jonas Ruh
Thibault Duretz
Production:
Mohamed Gouiza
Grace Shephard

Reviewers:
Andrea Tommasi
Manuele Faccenda

Submitted:
15 July 2025
Accepted:
11 May 2026
Published:
15 June 2026

1 Introduction

Geodynamic processes are greatly dependent on mantle viscosity, and yet this is one of the mantle's most enigmatic properties. Rock deformation experiments on mantle rocks reveal that viscosity is dependent on a large number of parameters, including temperature, pressure, strain, strain rate, grain size, water content, etc. (e.g. *Korenaga and Karato*, 2008). One of the less explored phenomena of mantle rheology is the anisotropic behaviour of viscosity, meaning that viscosity is not only dependent on strain rate but also on the direction and symmetry of the deformation. Anisotropic viscosity can arise from the layering of rocks with varying properties at the micro- or macro-scale, or from the integrated macroscopic impact of the anisotropic micromechanical behaviour of crystals.

1.1 Anisotropic Viscosity of Olivine

Olivine, the main rock-forming mineral in the upper mantle, has an orthorhombic crystal symmetry, which is characterised by intrinsic anisotropy. The crystallographic structure primarily affects the dislocation creep deformation mechanism, allowing for 50 times lower viscosity when deformation is produced by the weakest slip systems (shear parallel to the olivine [100] axis on the (001) or on the (010) planes) versus by the hardest slip system (shear parallel to the olivine [001] axis on the (010) plane) (*Durham and Goetze*, 1977). This micromechanical behaviour of olivine is best described using the critical resolved shear stresses on the different olivine slip systems, each of which contributes to deformation via dislocation creep. Based on *Hansen et al.* (2016a), the behaviour of olivine can be modelled assuming that in each grain there are three linearly independent slip systems that accommodate deformation: the (010)[100] and (001)[100] slip systems are relatively weak, with relative critically resolved stresses (t_0) of 0.3 and 0.27, respectively, and the (010)[001] slip system that is significantly stronger, with t_0=1.29. Deformation that cannot be produced by these slip systems is likely to occur on the grain boundaries instead. Note that these values were calibrated using experiments in which grain-boundary processes were active and are not expected to be equivalent to values determined in single-crystal experiments. Using these values therefore empirically includes the influence of those grain-boundary processes in the macroscopic behaviour, which is likely the case in upper-mantle deformation. In olivine aggregates, the magnitude of the macroscopic anisotropic behaviour depends on the texture of the aggregate. When grains of olivine are aligned with each other, and most of the easy slip planes are parallel to each other, the directional variations in viscosity can reach up to two orders of magnitude (*Hansen et al.*, 2016a).

Translating the micromechanical behaviour of individual olivine grains to a polycrystalline aggregate is not triv-

*✉ agnes.kiraly@geo.uio.no

ial. There are several models of homogenisation, including the Taylor and Sachs models, which assume homogeneous strain rate or homogeneous stress, respectively, among all of the crystals within an aggregate (*Sachs*, 1928; *Taylor*, 1938; *Hansen et al.*, 2016a). These two models provide the upper and lower bounds of the macroscopic mechanical behaviour. The visco-plastic self-consistent (VPSC) method provides a different approach, in which each grain is modelled within a separate conceptual homogeneous medium, resulting in a heterogeneous stress and strain rate distribution among the grains (*Lebensohn and Tomé*, 1993). The most accurate micromechanical modelling results can be obtained by full field models, however, their accuracy pairs with high computational costs (*Hansen et al.*, 2021). Independently of the homogenisation methods, micromechanical models allow us to relate macroscopic stresses to strain rates based on the integrated behaviour of individual grains. However, these models are impractical to include in large-scale geodynamic models, as they are computationally expensive and do not directly give information about the viscosity tensor (*Hansen et al.*, 2016a; *Signorelli et al.*, 2021).

1.2 Geodynamic Models with Anisotropic Viscosity

Experimental data on single olivine crystals (*Durham and Goetze*, 1977) and on olivine aggregates (*Hansen et al.*, 2012, 2016a,b) have inspired geodynamic modellers to explore the role of anisotropic viscosity within the asthenosphere and the lithospheric mantle using various degrees of simplification (e.g. *Christensen*, 1987; *Han and Wahr*, 1997; *Mühlhaus et al.*, 2003; *Lev and Hager*, 2011). The key modelling aspects involve: i) replacing the scalar viscosity in the constitutive equation that relates stress and strain rate with a rank-4 tensor viscosity, and ii) tracking the orientation and amplitude of the anisotropy across the modelling domain. For the upper mantle, this requires monitoring olivine textures (crystallographic preferred orientation – CPO) across the entire model domain, to compute anisotropic properties based on CPO orientation and magnitude, and tectonic stresses. This is hugely challenging in a geodynamic model, and therefore models with anisotropic viscosity usually implement some simplifications, such as transverse anisotropy, where different viscosity values are only used for vertical versus horizontal (or in-plane and plane-normal) deformations (*Christensen*, 1987; *Han and Wahr*, 1997; *Becker and Kawakatsu*, 2011). Similarly, models using the director method (*Mühlhaus et al.*, 2002) define two viscosities – a normal and a shear viscosity – while the orientation of the easy slip plane can rotate with the deformation. In both cases, the ratio between the two viscosity values is kept fixed and has often been inspired by the early experiments of *Durham and Goetze* (1977) ranging between 10 and 100. The director method has been applied to a variety of geodynamic situations, where viscous anisotropy is estimated from microscopic and macroscopic layering (*Lev and Hager*, 2008) or from olivine CPO (*Mühlhaus et al.*, 2003; *Becker and Kawakatsu*, 2011; *Lev and Hager*, 2011).

A different approach to decrease the model complexity is to model the anisotropic viscosity of olivine CPO but neglect the time evolution of the CPO and hence any changes in anisotropy. This is reasonable for processes that induce only small amounts of strain, such as the reactivation of lithospheric shear zones (e.g. *Mameri et al.*, 2020, 2023). More advanced models have included olivine CPO development and anisotropic viscosity. *Blackman et al.* (2017) developed a fully coupled flow-CPO-viscosity model for a small (2D flow) region of a mid-ocean ridge. However, in their models the CPO-related anisotropic viscosity only alters the effective viscosity by either hardening or weakening it, and thus the directional dependency of viscosity was not entirely considered. *Kiraly et al.* (2020) simultaneously evolved both the CPO and anisotropic viscosity tensors, but only for selected and generalised deformation paths, without any spatial variation of CPO. They used the modified director method (MDM) micromechanical model, based on the Taylor homogenisation scheme (*Hansen et al.*, 2016a), which required the calculation of stresses related to five different strain rate tensors in order to approximate the anisotropic fluidity tensor (inverse of the viscosity tensor). This step was necessary because the averaging between grains cannot be generalised from the stresses to the fluidity tensor. Their results were extrapolated to the asthenosphere for simplified representations of tectonic and geodynamic processes, such as changes in plate motion direction and subduction initiation. However, this approach cannot investigate complex geodynamic processes or the importance of the feedback with anisotropic viscosity for these complexities.

Nevertheless, the work by *Kiraly et al.* (2020) highlighted that evolving CPO and its associated anisotropic viscosity may exert first-order controls on geodynamic processes. Yet, due to computational challenges, it has not been possible to incorporate both CPO evolution and anisotropic viscosity into large-scale numerical models. In this paper, we present a new approach in which we devised a method to compute components of the anisotropic viscosity tensor directly from CPO parameters. This significantly simplifies an essential step that has so far eluded geodynamicists: defining the rank-4 viscosity tensor based on the CPO texture within a numerical model.

2 Methods

The simplest form of the (anisotropic) constitutive relationship between deviatoric stress and strain rate, using Einstein notation, is:

$$\sigma_{ij} = \eta_{ijkl} \cdot \dot{\varepsilon}_{kl}, \tag{1}$$

where η_{ijkl} represents the rank-4 viscosity tensor, including all dependencies on field parameters (e.g., temperature, pressure, strain, strain rate, CPO, water content, grain size, etc.), σ is the deviatoric stress and $\dot{\varepsilon}$ is the strain rate. Inverting this equation, we can define the fluidity tensor (ϕ):

$$\dot{\varepsilon}_{ij} = \phi_{ijkl} \cdot \sigma_{kl} \tag{2}$$

A single crystal of olivine has orthorhombic crystal symmetry, which means that its viscosity/fluidity tensor can be described by nine values. Polycrystalline olivine aggregates, in the most general case, have a triclinic symmetry (with 21 independent viscosity parameters). However,

when the mean orientations of the olivine axes are parallel to the model reference frame, the anisotropic viscous behaviour can be approximated by orthotropic symmetry, similar to a single crystal (*Signorelli et al.*, 2021). In this case, the fluidity tensor can be expressed with the help of the orthotropic Hill yield criteria (*Hill*, 1948; *Signorelli et al.*, 2021), applied for creep deformation (*Bhatnagar and Gupta*, 1967), where the stress invariant (σ_I) is defined equivalent to the square root of the plastic potential (f); i.e. $f = {\sigma_I}^2$. Thus, the orthotropic stress invariant is defined as:

$$\sigma_I = \sqrt{\frac{2}{3}}\Big(F\left(\sigma_{22}-\sigma_{33}\right)^2 + G\left(\sigma_{33}-\sigma_{11}\right)^2 + H\left(\sigma_{11}-\sigma_{22}\right)^2 + 2L\sigma_{23}^2 + 2M\sigma_{13}^2 + 2N\sigma_{12}^2\Big)^{1/2}, \tag{3}$$

where *F, G, H, L, M,* and *N* are the so-called Hill coefficients. *Bhatnagar and Gupta* (1967) expanded the relationship between strain increments and stress in conjunction with the yield criterion ($d\varepsilon_{ij} = \frac{\partial f}{\partial \sigma_{ij}} d\lambda$; *Hill*, 1948, where $d\lambda$ is a positive, scalar factor of proportionality) to strain rates:

$$\dot{\varepsilon}_{ij} = \frac{\dot{\varepsilon}_I}{\sigma_I} \cdot \frac{\partial f}{\partial \sigma_{ij}}, \tag{4}$$

which allows us to formulate a constitutive equation for orthotropic materials. In equation (4), $\dot{\varepsilon}_I$ is the strain rate invariant that can be defined by different types of flow laws. For dislocation creep, a form of Norton's law of $\dot{\varepsilon}_I = \gamma {\sigma_I}^n$ can be applied (*Bhatnagar and Gupta*, 1967). The combination of equations (3) and (4) applied to dislocation creep gives us the anisotropic form of constitutive equation between the viscous strain rate and the deviatoric stress tensors for orthotropic materials (*Hill*, 1948; *Bhatnagar and Gupta*, 1967; *Signorelli et al.*, 2021):

$$\dot{\varepsilon}_{ij} = \gamma_0 e^{(-Q/RT)} {\sigma_I}^{n-1} \cdot A_{ijkl} \cdot \sigma_{kl} \tag{5}$$

where γ_0 is experimentally derived isotropic fluidity [$Pa^{-n}s^{-1}$], Q is the activation energy, n is the power-law exponent, and $\boldsymbol{A}$ is the rank-4 anisotropy tensor for fluidity that expresses the anisotropic fluidity properties of the olivine aggregate, and which, in Kelvin notation, takes the following form:

$$\mathbf{A_{Kelvin}} = \frac{2}{3}\begin{bmatrix} G+H & -H & -G & 0 & 0 & 0 \\ -H & H+F & -F & 0 & 0 & 0 \\ -G & -F & F+G & 0 & 0 & 0 \\ 0 & 0 & 0 & L & 0 & 0 \\ 0 & 0 & 0 & 0 & M & 0 \\ 0 & 0 & 0 & 0 & 0 & N \end{bmatrix} \tag{6}$$

The notations of the Hill coefficients in this work are derived from the original paper from *Hill* (1948), and thus are different from the notations used in *Signorelli et al.* (2021). It is important to note, that equations (3-5-6) are only valid for an olivine polycrystal when our reference frame is aligned with the mean CPO orientation.

2.1 CPO Reference Frame and Texture Characterisation with Bingham Statistics

Anisotropic viscous behaviour can be expressed using equation (5) if the model reference frame is aligned with the principal axes of anisotropy, which can be defined as the orthogonal frame defined by the mean orientation of the olivine symmetry axis (*Signorelli et al.*, 2021; *Mameri et al.*, 2020). We define the mean CPO orientation using the eigenvectors related to the largest eigenvalues of the second-order orientation tensor (or covariance matrix) for each symmetry axis. Because the three symmetry axes are handled independently, we additionally correct the [010]- and [001]-axes orientations to ensure that they form an orthogonal basis with the mean [100]-axis orientation (Text S1, Figure S1). The three eigenvalues of the second-order orientation tensor (or covariance matrix) for each axis contain information about the dispersion of orientations around the mean orientation (*Bingham*, 1974). However, one must be careful, as Bingham statistics of the second-order orientation tensor only provide reliable information about the texture for cases in which only one point maximum is present. In the following, we refer to eigenvalues of the orientation tensor of the olivine symmetry axis ([100] ≡ a, [010] ≡ b, [001] ≡ c) as texture parameters (*named a_i, b_i, c_i; i:1,2,3*) and the matrix of the corrected maximum eigenvectors as the CPO rotation matrix.

2.2 Search for the Hill Coefficients

The anisotropic viscosity (and fluidity) tensor is a stress-dependent variable, as it depends on both the amplitude and the orientation of the stress with respect to the CPO. By contrast, the Hill coefficients (equations 3 and 6) are characteristic material parameters that only depend on the CPO of the polycrystalline material and the relative strengths of the slip systems that accommodate deformation. These coefficients have some constraints given by the orthotrophic plasticity theory: i) for isotropic materials F=G=H=0.5 and L=M=N=1.5, ii) L, M, and N must be positive, while F+G, G+H, H+F must be positive, which implies that at most one out of the three can be negative (*Hill*, 1948). To determine the Hill coefficients of a given texture, we use the polycrystal equipotential surface analysis (*Signorelli et al.*, 2021; *Christodoulou and Tomé*, 2025). For this analysis, it is useful to represent the stress and strain rate tensors as linear combinations of the orthonormal symmetric b-basis tensors (Appendix B in *Signorelli et al.*, 2021). In this b-basis, the stress (S) and strain rate tensors are represented by 6-component vectors:

$$\begin{aligned} S_b &= (S_1, S_2, S_3, S_4, S_5, S_6) \\ &= \left(\frac{S_{22}-S_{11}}{\sqrt{2}}, \frac{2S_{33}-S_{22}-S_{11}}{\sqrt{6}}, \sqrt{2}S_{23}, \right. \\ &\qquad \left. \sqrt{2}S_{13}, \sqrt{2}S_{12}, \frac{S_{33}+S_{22}+S_{11}}{\sqrt{3}}\right) \end{aligned} \tag{7}$$

The deviatoric stress (σ) in the b-basis simplifies to:

$$\sigma_b = (\frac{\sigma_{22}-\sigma_{11}}{\sqrt{2}}, \sqrt{\frac{2}{3}}\sigma_{33}, \sqrt{2}\sigma_{23}, \sqrt{2}\sigma_{13}, \sqrt{2}\sigma_{12}, 0) \quad (8)$$

The same can be applied to the strain rate for incompressible materials. Using the b-basis components to plot the equipotential surfaces of a polycrystal (PES) is meaningful because in this case, the normal at any stress point is the corresponding strain rate (*Christodoulou and Tomé*, 2025). Further, in specific sub-spaces of the b-bases,where the material is subjected to deformation that can be reduced to only two components of the b-basis vector, equipotential surfaces reduce to ellipses. We call these Hill-ellipses, as their semi-major and minor axes, and their tilt, are directly related to the Hill coefficients. If we express the plastic potential in the b-basis (*Christodoulou and Tomé*, 2025) we find that:

$$2f = \frac{F+4H+G}{2}{\sigma_1}^2 + \frac{3(F+G)}{2}{\sigma_2}^2 + \sqrt{3}(G-F)\sigma_1\sigma_2 + L{\sigma_3}^2 + M{\sigma_4}^2 + N{\sigma_5}^2 = \text{const.} \quad (9)$$

In the $(\sigma_1 - \sigma_2)$ subspace, which defines the commonly used π-plane representation, equation (9) reduces to

$$2f = \frac{F+4H+G}{2}{\sigma_1}^2 + \frac{3(F+G)}{2}{\sigma_2}^2 + \sqrt{3}(G-F)\sigma_1\sigma_2, \quad (10)$$

which is the equation of a centered, tilted ellipse (Figure 1, top left panel). In this case, the Hill coefficients relate to the ellipse parameters as follow:

$$\frac{F+4H+G}{4{\sigma_0}^2} = \left(\frac{\cos^2\theta}{a^2} + \frac{\sin^2\theta}{b^2}\right), \quad (11a)$$

$$\frac{3(F+G)}{4{\sigma_0}^2} = \left(\frac{\sin^2\theta}{a^2} + \frac{\cos^2\theta}{b^2}\right), and \quad (11b)$$

$$\frac{\sqrt{3}(G-F)}{(2\sigma_0)^2} = \sin(2\theta)\left(\frac{1}{a^2} - \frac{1}{b^2}\right). \quad (11c)$$

In equations (11a–c), (11a) and (11b) are the semi-major and the semi-minor axes of the tilted ellipse, respectively, θ is the tilt angle, and σ_0 is a constant that is proportional to the radius (r) of the equipotential surface of an isotropic aggregate (which is a circle): $\sigma_0 = \sqrt{\frac{3}{4}}r$.

In shear planes (e.g. in the in $(\sigma_1 - \sigma_3)$ subspace) the PES plots as a centered, axis-aligned ellipse (Figure 1), and hence, the ellipse's semi-major and semi-minor axes are related to the Hill coefficients (in $(\sigma_1 - \sigma_3)$, subspace)as:

$$\frac{a}{b} = \sqrt{\frac{2L}{F+4H+G}} \quad (12)$$

Thus, if we find the ellipse parameters in the $(\sigma_1 - \sigma_2)$, $(\sigma_1 - \sigma_3)$, $(\sigma_1 - \sigma_4)$, and $(\sigma_1 - \sigma_5)$ subspaces for a polycrystal with a given CPO, we can determine its Hill coefficients. For this, we utilise the PCYS (polycrystal yield surface) subroutine in VPSC (*Lebensohn and Tomé*, 1993) in the $(\sigma_1 - \sigma_2)$ subspace, and further test the polycrystal's response to simple shearing in the b-bases 3-, 4-, and 5-directions. These tests provide a set of input strain rate and modelled stress pairs. The simple shear results in combination with the PCYS results provide us with the semi-major and semi-minor axes of the axis-aligned ellipses in the shear-plane projections, while the PCYS test in the $(\sigma_1 - \sigma_2)$ subspace provides data points to which we can fit a tilted ellipse in the π-plane projection. We estimate the error of the fit using equation (5) to predict strain rate from the resulting VPSC stresses, and compare those with the input strain rate. The error is defined as:

$$\text{Error} = \text{mean}\left(\frac{|\|\dot{\varepsilon}_{\text{VPSC input}}\| - \|\dot{\varepsilon}_{\text{predicted}}\||}{\|\dot{\varepsilon}_{\text{VPSC input}}\|}\right). \quad (13)$$

In the VPSC simulations (*Lebensohn and Tomé*, 1993), we use the affine linearisation scheme, with the slip system parameters listed in Table 1. This choice was based on computational cost and the shape of the polycrystal equipotential surfaces in the π- and shear-plane projections. After comparing the VPSC linearisation schemes (*de Oliveira*, 2020), we conclude that the tangent approximation often leads to convex equipotential surfaces which would lead to serious issues in the ellipse fitting. The affine approximation predicts fairly smooth ellipse surfaces, but higher stresses than the second-order approximation. However, the ratios between the ellipse axes are not significantly different between the two methods. The higher stresses can be negotiated by using smaller critical resolved shear stress (CRSS) values for the fictional pyramidal slip systems (*Mameri et al.*, 2019) that allow for isotropic deformation (last three rows in Table 1). The CRSS values in this study also differ from *Mameri et al.* (2019) in the relative strength of the [001](010) slip system, referencing the MDM method based on the laboratory experiments by *Hansen et al.* (2012, 2016b,a). These laboratory tests were done on dry olivine at high temperature but with small grain sizes. Although the average grain size in the experiments is 2-3 orders of magnitude lower than what we expect in the asthenosphere, extrapolation of existing flow laws to geological conditions suggests the same deformation mechanisms are occurring in these experiments as in the asthenosphere (*Kohlstedt and Hansen*, 2015), thus the implications of the laboratory tests are relevant for asthenospheric mantle conditions.

2.3 Building a Database

Our ultimate aim is to build a database of textures with their best fitting Hill coefficients. This will enable us to link the Hill coefficients directly to the texture parameters, i.e. to the eigenvalues of the mean second-order orientation tensors. This method could then be used with any selected texture evolution model. With this purpose in mind, we constructed a database that includes textures computed by tracking deformation on passive tracers in five different geodynamic

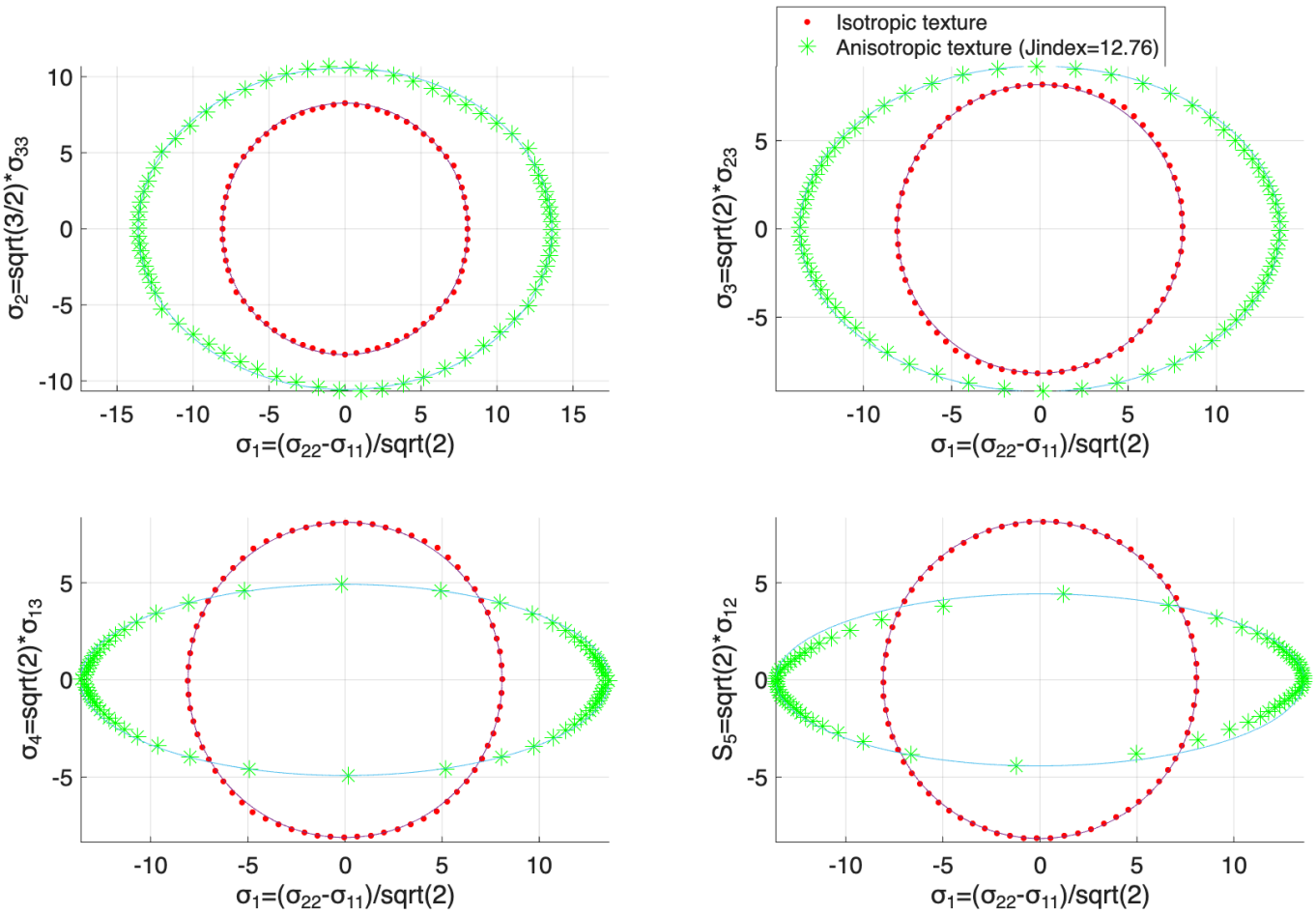

FIGURE 1 – Equipotential surfaces plotted for PCYS analyses in the (σ_1- σ_2), (σ_1- σ_3), (σ_1- σ_4), and (σ_1- σ_5) planes, for an isotropic and an anisotropic texture (with J index = 12.76), together with the fitted ellipses. The anisotropic texture is comparable to the one used in *Signorelli et al.* (2021). Here, the Hill coefficients derived from the best fitting ellipses for the anisotropic texture are: F=0.296, G=0.309, H=0.119, L=1.182, M=4.147, N=5.109.

TABLE 1 – The olivine slip systems, their relative critical resolved shear stress (CRSS) values and stress exponents used in the VPSC models. Comparisons between our VPSC setup against the one used in (*Mameri et al.*, 2019) and against laboratory experimental data (*Hansen et al.*, 2012, 2016b) are shown in the Supporting Information Figure S2.

Slip Systems	Relative CRSS	Stress exponent
[100](010)	1	3
[100](001)	1	3
[001](010)	4	3
[001](100)	10	3
[100](011)	10	3
[001](110)	10	3
<110>{111}	30	3
<011>{111}	30	3
<101>{111}	30	3

models, including a Stokes sinker, a corner flow model (presented in *Fraters and Billen*, 2021), and advancing and retreating subduction models (*Wang et al.*, 2025). All of these geodynamic models were run in ASPECT (*Bangerth et al.*, 2024) using the D-Rex (*Kaminski et al.*, 2004) based CPO implementation from *Fraters and Billen* (2021) (Figure S2). We further included textures from a simple shear model that used MDM for the texture evolution (*Hansen et al.*, 2016a; *Kiraly et al.*, 2020), from laboratory experiments (*Hansen et al.*, 2012, 2016b), as well as textures generated within MTEX using the Bingham Distribution function (*Mainprice et al.*, 2015). Within the ASPECT models, tracers reach strains up to 14, while the simple shear model reaches a strain of 21. This exercise results in a database of a variety of textures produced by a range of models/methods that might occur in nature and that might be encountered in 4D geodynamic models.

In the database for each texture we include the best-fitting Hill coefficients (computed as described in section 2.2), the error associated with those Hill coefficients (equation 13), and several parameters that describe the texture. These parameters include the M- and J-indices (*Skemer et al.*, 2005; *Mainprice et al.*, 2015), the eigenvalues of the covariance matrices for the three principal axes of olivine ([100], [010], and [001] axes) normalised by the number of grains, and the euler angles of the mean CPO reference frame. From the eigenvalues we can also calculate the P (pointiness), G (girdle-ness), and R (randomness) scores of the textures (*Vollmer*, 1990).

2.4 Linear Regression Models Between Texture Parameters to Hill Coefficients

We filter outliers from the database where textures with Hill coefficients of very poor confidence (Error >0.25) are removed. We then run linear regression models on the Hill coefficients and several combinations of texture parameters with a weight based on the Hill coefficients' error (equation 13). Since this step is computationally inexpensive, we tested several combinations of the eigenvalues of the orientation tensors (see details in Table 2), based on visual evaluations between individual Hill coefficients plotted against each texture parameter (e.g. the pointiness of the [100] axis in Figure 3).

3 Results

3.1 Database

The filtered database consists of 17,355 "samples". These textures span from random (i.e., isotropic) textures to well-developed high-strain textures with a maximum M-index (*Skemer et al.*, 2005) of 0.84 and maximum J-index (*Mainprice et al.*, 2015) of 52. The mean values for the M- and J-indices are 0.24 and 6.2, respectively. The textures included in the database cover almost the entire P-G-R space for all three symmetry axes (Figure 2). On average, we are able to determine the anisotropy parameters—the Hill coefficients—with good confidence, with a mean error of 7.9%. The Hill coefficients F, G, and H have a general decreasing trend with increasing M-index and the increasing pointiness of the [100] axis, while M and N have a non-linear increasing trend with increasing pointiness of the [100] axis (Figure 3). Hill coefficient L has no clear trend with the pointiness of the [100] axis, despite a somewhat increasing trend as a function of the M index. Orange stars mark the Hill coefficients of the most isotropic texture from our database (M index ~10^{-4}) in Figure 3, showing values very close to the theoretical isotropic values. Further, Hill coefficients in our database are all positive, complyng with the constraints described above.

3.2 Linear Regression Models

We use linear regression models on eight different combinations of texture parameters to predict the corresponding Hill coefficients (*F, G, H, L, M, N*) from our database. We refer to the resulting transfer functions as CPO2Hill models *v1-8* (Table 2). While all combinations provide a reasonably good fit (with $R^2 \geq 0.76$), the best fit was found for models where the largest eigenvalues of all three axes are used in at least a quadratic relationship, while the smallest eigenvalues are used in linear (v2, v8) or inverse (v3) relationships, with R^2=0.84-0.86, (Table 2 and Figures S-11). This is also shown in Figure 4, where we plot the mean distance between the modelled and the database values, normalised by the range of each Hill coefficient along with the standard deviation of this fit.

3.3 Testing Model Results Against Laboratory Data

In the previous section, we showed that each linear regression model reproduces the database with a reasonably good fit, however, the best fit is produced by CPO2Hill model v3. Here, we test these models against measurements of viscous anisotropy obtained in laboratory rock deformation experiments (*Hansen et al.*, 2012, 2016b). We compare the equivalent strain rate values normalised by the value obtained for an isotropic texture in the laboratory during rock deformation experiments on aggregates of Fo_{50} olivine in extension and torsion, with the normalised equivalent strain rates modelled using the CPO2Hill models. For the modelling, we applied an equivalent stress of 1 MPa, which means

$$\sigma_{ext} = \begin{pmatrix} -\frac{1}{3} & 0 & 0 \\ 0 & \frac{2}{3} & 0 \\ 0 & 0 & -\frac{1}{3} \end{pmatrix} \text{ and } \sigma_{shear} = \begin{pmatrix} 0 & \sqrt{\frac{1}{3}} & 0 \\ \sqrt{\frac{1}{3}} & 0 & 0 \\ 0 & 0 & 0 \end{pmatrix}$$

for input stress tensors, mimicking the laboratory data in extension and in torsion, respectively. To be comparable, laboratory strain rates were rescaled to a unit equivalent stress following (*Mameri et al.*, 2019):

$$\dot{\varepsilon}^*_{eq} = 1^{4.1} \frac{\dot{\varepsilon}_{eq}}{{\sigma_{eq}}^{4.1}} \tag{14}$$

The Supporting Information (Figures S12-19) includes plots of each CPO2Hill model prediction plotted together with the laboratory data. To summarise all the results, we show here the predicted amplitudes of anisotropy for samples that were tested in both extension and torsion, including samples that were initially untextured or pretextured in extension or torsion. Figure 5 shows results of laboratory

TABLE 2 – Linear regression models CPO2Hill v1-v8. Each model is a linear combination (Lin) of the listed texture parameters, where $a_{1..3}$, $b_{1..3}$, and $c_{1..3}$ are the eigenvalues (from largest to smallest) of the mean orientation tensor of the [100], [010], and [001] axes. For each linear regression model the R2 (root mean square, or goodness of fit) is listed. In addition, we detail the mean distance between the modelled and the database values of each Hill coefficient, which we normalised by the range of the given Hill coefficients in the database for better comparision (Figure 4).

CPO2Hill v1	Lin(a_1, a_2, a_3, b_1, b_2, b_3, c_1, c_2, c_3)					
R2	0.76	F -	0.042	G -	0.050	H - 0.032
Normalised misfit for:		L -	0.035	M -	0.024	N - 0.047
CPO2Hill v2	Lin(a_1^2, a_1, a_2, a_3, b_1^2, b_1, b_2, b_3, c_1^2, c_1, c_2, c_3)					
R2	0.84	F -	0.040	G -	0.044	H - 0.030
Normalised misfit for:		L -	0.030	M -	0.019	N - 0.028
CPO2Hill v3	Lin(a_1^2, a_1, a_2, $1/a_3$, $b1^2$, b_1, b_2, $1/b_3$, c_1^2, c_1, c_2, $1/c_3$)					
R2	0.86	F -	0.040	G -	0.044	H - 0.030
Normalised misfit for:		L -	0.030	M -	0.016	N - 0.025
CPO2Hill v4	Lin(a_1^2, a_2, a_3, b_2, b_3, c_2, c_3)					
R2	0.81	F -	0.041	G -	0.044	H - 0.031
Normalised misfit for:		L -	0.036	M -	0.022	N - 0.032
CPO2Hill v5	Lin($a1^4$, a2, a3, b2, b3, c2, c3)					
R2	0.81	F -	0.042	G -	0.044	H - 0.032
Normalised misfit for:		L -	0.035	M -	0.021	N - 0.032
CPO2Hill v6	Lin($a1^4$, a_1^2, a_2, a_3, b_2, b_3, c_2, c_3)					
R2	0.82	F -	0.041	G -	0.044	H - 0.029
Normalised misfit for:		L -	0.035	M -	0.020	N - 0.032
CPO2Hill v7	Lin(a_1, a_2, a_3, b_1, b_2, b_3, $1/c_1$, c_2, c_3)					
R2	0.81	F -	0.042	G -	0.045	H - 0.032
Normalised misfit for:		L -	0.034	M -	0.020	N - 0.039
CPO2Hill v8	Lin(a_1^4, a_1, a_2, a_3, b_1^2, b_1, b_2, b_3, c_1^2, c_1, c_2, c_3)					
R2	0.84	F -	0.040	G -	0.044	H - 0.031
Normalised misfit for:		L -	0.031	M -	0.019	N - 0.027

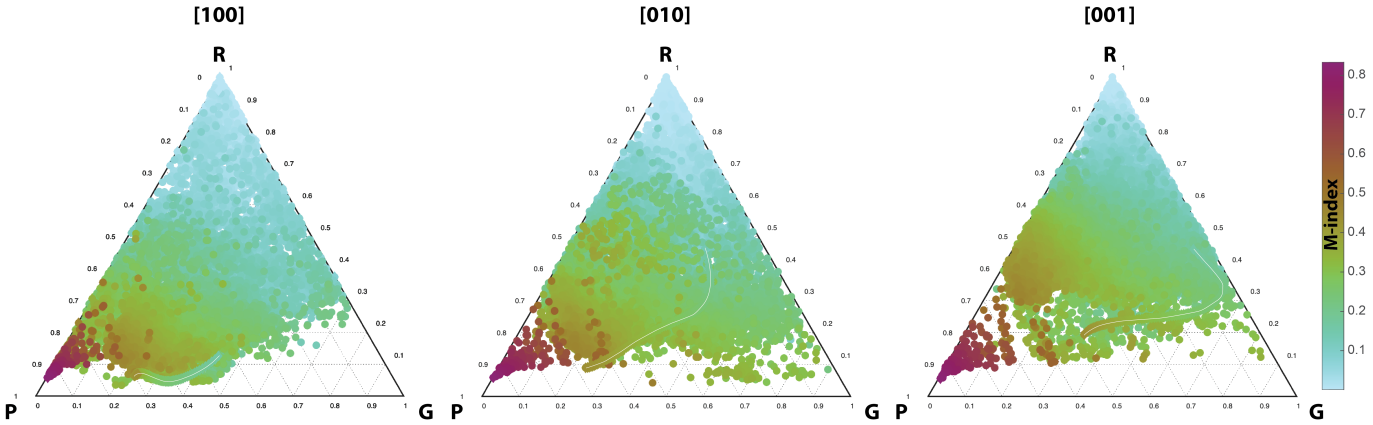

FIGURE 2 – P-G-R space covered by the filtered database, plotted in three panels for each olivine axis. Each point represents a texture in the database and is coloured based on the texture's M-index. Thin white lines show the evolution of a texture in simple shear between shear strains of 2 and 11, based on model 1 from *Kiraly et al.* (2020).

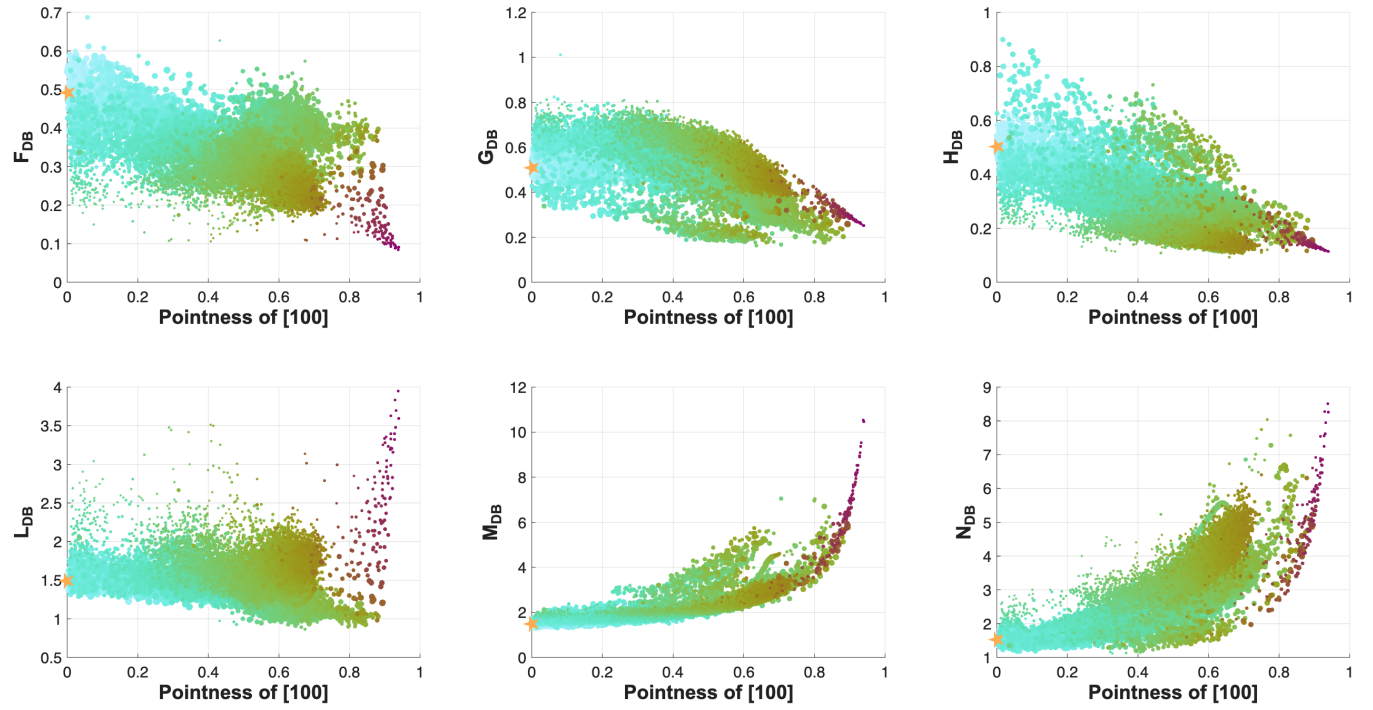

FIGURE 3 – Hill coefficients in the database plotted against the pointiness score of the [100] axis. The datapoints are coloured according to the average texture score (M index) and size-scaled according to the inverse of the error of the fitted Hill coefficients (equation 13). Orange stars mark the Hill coefficients of an isotropic texture (M index~10^{-4}).

experiments, VPSC simulations, and CPO2Hill models. The magnitude of anisotropy is the ratio between the viscosity measured in extension and the viscosity measured in torsion (*Hansen et al.*, 2012). Here, we use the equivalent strain rates that are scaled to a unit stress (for laboratory data and CPO2Hill models) and the equivalent stresses scaled to a fixed strain rate (for laboratory data and VPSC models) to calculate the magnitude of anisotropic viscosity:

$$M_{AV} = \left(\frac{\dot{\varepsilon}_{shear}}{\dot{\varepsilon}_{extension}} \right)^{\frac{1}{n}} = \frac{\sigma_{extension}}{\sigma_{shear}} \qquad (15)$$

Comparing model predictions with laboratory data and with VPSC simulations, we find a reasonable correlation between increasing anisotropy and increasing texture index. However, as for the VPSC models, the CPO2Hill models also overestimate the amplitude of anisotropy at higher strains (higher M index textures). Comparing CPO2Hill predictions, we find that CPO2Hill models v2, v3, and v8 produce results closest to the laboratory data and to the VPSC simulations (Figure 5, Supplementary Figures S11, S12, S18).

3.4 Testing CPO2Hill Models in Simple Shear

Based on the best fitting models for each of the Hill coefficients (Table 2, Figure 4), and the tests against laboratory data, we further test CPO2Hill models v2, v3, v6, and v8 in simple shear experiments, where we apply a shear stress of 1 unit in the x-direction on the z-normal plane for an initially uniform texture. At each timestep, the input stress is rotated to the CPO reference frame, where the anisotropic tensor for fluidity, the anisotropic stress invariants, and the strain rates are calculated via equation (5), based on the Hill coef-

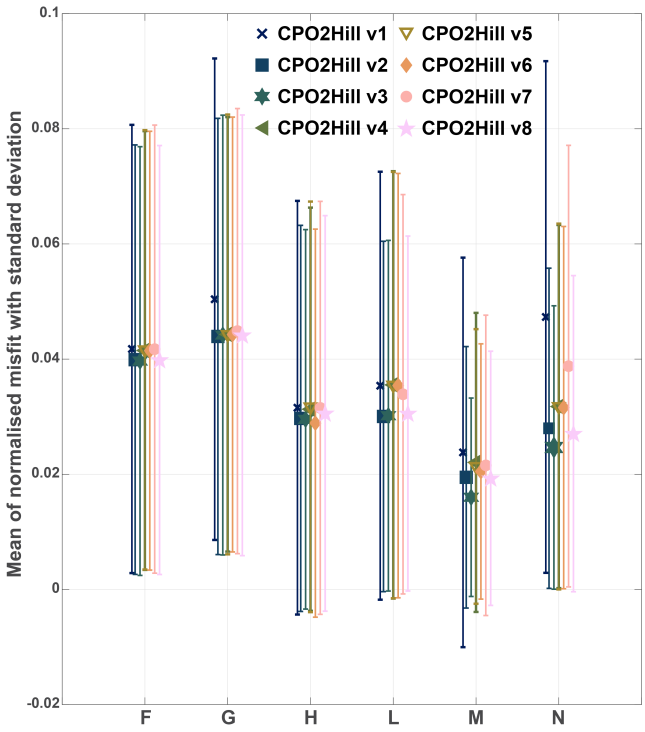

FIGURE 4 – CPO2Hill model misfits for each Hill coefficient, calculated as the mean distance between the modelled and the database values, normalised by the range of each Hill coefficient in the database. Detailed description of CPO2Hill models v1-v8 are in Table 2. For each model, the normalised mean misfit is represented by a symbol, and the standard deviation from the mean normalised misfit is represented by a vertical line.

ficients predicted by the given CPO2Hill model. The strain rate is then back-rotated to the model reference frame, and used to determine the velocity gradient tensor, which is then used in the MDM texture evolution model. For each texture produced in our model using MDM, we compare the CPO2Hill strain rates with the ones predicted by VPSC, where we imposed the same stress and boundary conditions that we applied for the CPO2Hill models, and used with the slip system parameters listed in Table 1.

The results show that in all models we slightly overpredict the weakening of textures with low strains (between 0.5-1.5) and underpredict it at medium-high strains with respect to the VPSC simulations (Figure 6A). In this simplest model, where the shear stress is uniform throughout the test, the CPO2Hill model v3 predictions are the closest to the VPSC results. With respect to earlier models (*Kiraly et al.*, 2020), the maximum strain rate occurs at slightly smaller strains (~5 vs ~8), but the general trends are similar. We also found that the texture evolution is not affected by the choice of the CPO2Hill model version during the simple shear models (evidenced by the equal VPSC prediction for the textures evolving with the different CPO2Hill models, Figure 6). The resulting textures are also in agreement with previous modelling results and laboratory experimental results (*Hansen et al.*, 2016a; *Kiraly et al.*, 2020; *Wang et al.*, 2024). We also test the effect of abruptly changing the shear stress, mimicking the models of *Kiraly et al.* (2020), where the F_1 driving force was abruptly changed to F_2 or F_4, representing a change in plate pull force or the development of a vertical shear zone parallel to the previous plate motion, respectively. In these tests, where the sense of shear is changed either to the x direction on the y-normal plane (Figure 6B) or the y direction on the z-normal plane (F1 to F4 and F1 to F2, resp., in *Kiraly et al.* (2020)), CPO2Hill model v3 is still the best overall performing model. However, in the model where we change the shear plane (similar to F1 to F4, in *Kiraly et al.* (2020), Figure 6B) CPO2Hill model v6 and v8 perform the best at higher strains. When we change the shear direction (similar to F1 to F2, in *Kiraly et al.* (2020), Figure 6C), none of the models evolve similarly to the VPSC models, while the long-lasting hardening effect and the evolving texture is in agreement with the results in *Kiraly et al.* (2020). When comparing to the models of *Kiraly et al.* (2020), it is also worth noting that the computation time for a timestep in these simple shear models using the CPO2Hill method is reduced by a factor of more than 20.

4 Discussion

The results presented above demonstrate a new method to greatly simplify models of anisotropic viscous flow by inferring the anisotropic viscous parameters directly from the CPO of olivine. Our use of a variety of geodynamic simulations to create a database of relevant (static) textures allowed us to base our method on a broad representation of possible textures (Figures 2, 3). Using equation (5) (*Signorelli et al.*, 2021), for every texture in the database we have found a set of Hill coefficients that best fit the anisotropic viscosity predicted by the VPSC micromechanical model (*Lebensohn and Tomé*, 1993) for a large range of strain rates (in four specific subplanes). We note that the Hill coefficients for a texture formed in simple shear (with J-index ~12.7, Figure 1) are somewhat different in our study than the ones reported previously based on VPSC modelling (*Signorelli et al.*, 2021; *Mameri et al.*, 2020). This is likely due to the different linearisation scheme and critical resolved shear stresses for olivine slip systems used in the VPSC computations, as well as the different definitions we used for the stress invariant (equation 3) and for the anisotropic tensor for fluidity (equation 6). We derived our equations strictly following the convention in *Hill* (1948), while the previous VPSC models had a different definition of the Hill coefficients (see equations 8 and 10 in *Signorelli et al.*, 2021). This discrepancy highlights that the absolute values of the Hill coefficients, and thus the anisotropic behaviour, are strongly dependent on the assumptions made to link the relative strengths of single crystal mechanical behaviour to overall anisotropic behaviour of the homogenised textures. Nevertheless, our overarching method to link rock texture to viscous anisotropy is internally robust, and can be adapted to other methods defining the Hill coefficients.

In the database, the best-fitting Hill coefficients reproduce the strain rates applied in the micromechanical model with an average error (equation 13) of 7.9%. We note that the textures with the highest misfit, which are not considered in the final database, either have a complex pattern, such as with multiple maxima, or a high J-index (and high strain) from the simple shear model. In the first case, the texture may not be adequately described using Bingham statistics, which uses eigenvalues of the second-order orientation tensor that are better adapted to describe single max-

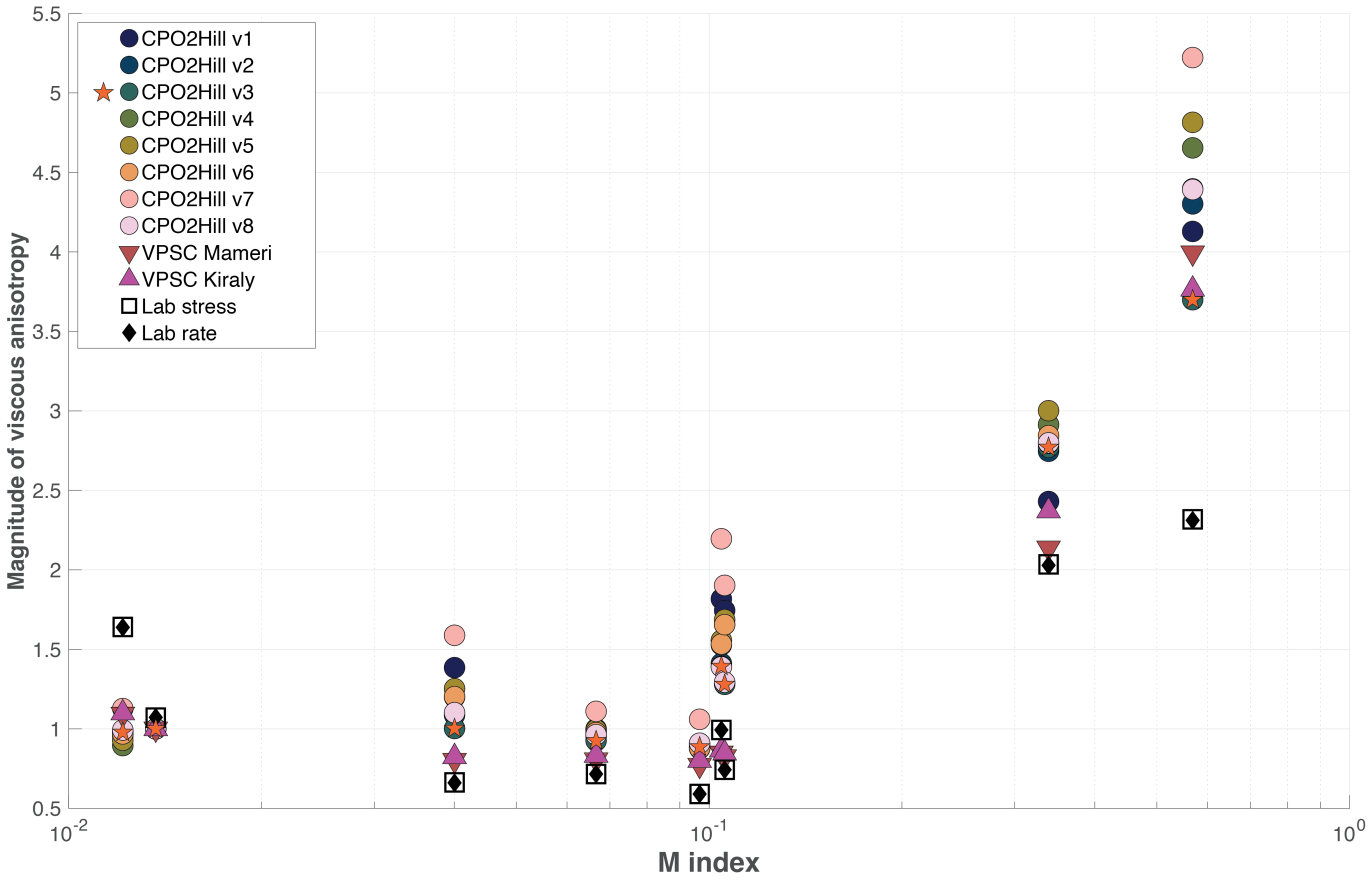

FIGURE 5 – Magnitude of anisotropy of textures that were both deformed in extension and in torsion, plotted against the overall strength (M index) of the textures. The magnitude of viscous anisotropy is equivalent when derived from scaled strain rates (black diamonds) or scaled stresses (black squares) measured in laboratory experiments. Triangles show results from VPSC simulations that use the relative slip system activities in *Mameri et al.* (2019) (salmon colour), and the relative slip system activities used in this study (Table 1, purple colour). Filled circles represent the results of the CPO2Hill models. Orange stars mark the best CPO2Hill model (v3).

ima and girdle textures. In the future, we can improve on the first point by using a more complete description of textures with higher order orientation tensors or harmonic degrees (*Rathmann et al.*, 2024), although defining the mean CPO reference frame will continue to be a challenge (Supporting Information Text S1, Figure S1). For textures with high strain, we note that the PCYS analysis in VPSC results in somewhat distorted ellipses, and thus the constrained ellipse parameters might not create a smooth fit with the data. It is possible that using a higher order linearisation scheme could rectify this problem, but using a second-order approximation is too costly for building a database with several thousands of textures. Thus, we conclude that the CPO2Hill method works well within the assumptions that the modelled textures do not reach strains higher than ~10-14 and can be approximated as an orthotropic material. Our database suggests that most textures that occur in geodynamic simulations stay within the limits where this assumption is reasonable. Furthermore, the specific coefficients of the CPO2Hill models are dependent on the micromechanical model setup that we used to calculate the Hill coefficients. Our VPSC setup reproduces reasonably well the laboratory results (Figure 5, Figure S3), which were performed on dry, fine grained olivine aggregates at high temperature and moderate pressure. This setup also reproduces well the previous VPSC simulations (Figure 5, Figure S3, *Mameri et al.*, 2019) that were set out to model anisotropic viscosity in the lithospheric and asthenospheric mantle.

Linear regression models (CPO2Hill models v2, v3, v6, and v8) yield similarly good fits between the database's Hill coefficients and those calculated from texture parameters (R^2~0.82-0.86), and reproduce the main trends observed in laboratory experiments. In simple shear, CPO2Hill v3 agrees best with the VPSC calculation and with earlier MDM-based simple shear models (*Kiraly et al.*, 2020). All four CPO2Hill models that we tested predict similar texture evolutions to the ones reported in *Kiraly et al.* (2020), and these are comparable to textures from torsion experiments (*Hansen et al.*, 2016b). The similar texture evolution among the CPO2Hill models explains why the VPSC calculations are nearly equivalent for all CPO2Hill models (Figure 6A-C).

When the shear direction is changed from shearing along the x-direction on the z-normal plane to shearing along the y-direction on the z-plane, the VPSC simulations and CPO2Hill simulations diverge (Figure 6C). We explain this divergence by the nature of the evolving texture. As the CPO rotates towards the new shear direction, the pattern becomes somewhat complex, especially for the [010] and the [001] axes. This means that the definition of the CPO reference frame becomes poorly defined and thus problematic for our implementation. Specifically, we are applying the orthotropic equations to a system that in the defined CPO reference frame might not be orthotropic. As a test,

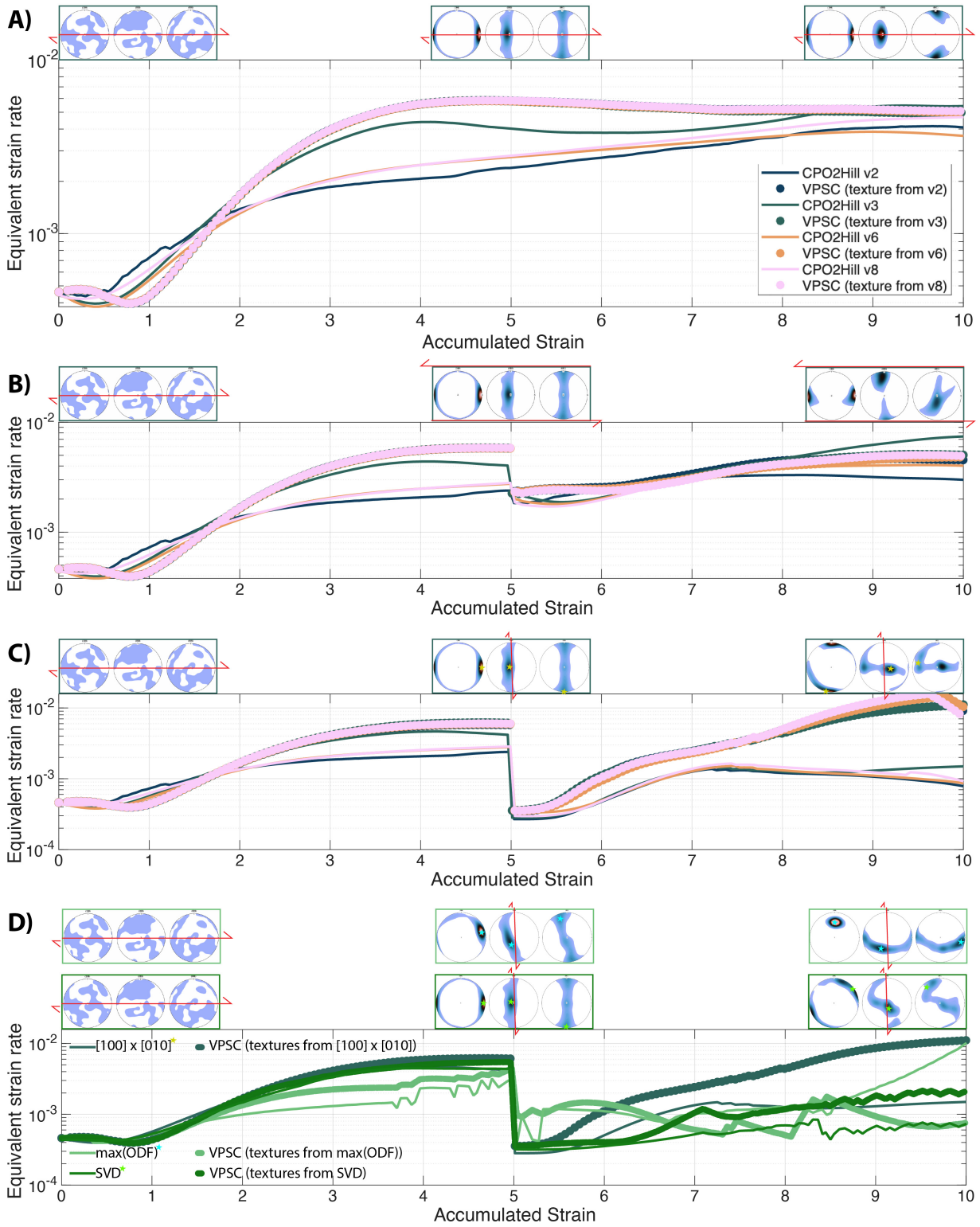

FIGURE 6 – Simple shear test using the CPO2Hill models. Solid lines show the evolution of the equivalent strain rate using different CPO2Hill models, while circles show the corresponding strain rates simulated with VPSC, as a response to a unit stress in A) the x direction on the z plane; B) the x direction on the z plane followed by the x direction on the y plane; C and D) the x direction on the z plane followed by the y direction on the z plane. In D) we explore the influence of the method of calculating the CPO reference frame. The darkest green line is the same as the CPO2Hill v3 model in panel C), which uses the eigenvectors of the second-order orientation tensor, and corrects for orthogonality using the cross products of the [100] and [010] eigenvectors. The other two shades of green show the evolution using the max(ODF) or the SVD methods, respectively. We show pole figures of the orientation distribution with the sense of shear stress in the CPO2Hill model v3 at strains of 0, 5.1, and 10. The textures evolving in the other CPO2Hill models are very similar to the ones shown for panel A)-C). In panel D) the top row shows how the texture evolves when using the max(ODF) method to calculate the CPO reference frame, while the second row shows textures evolving with the SVD method. In the pole figures of panels C) and D) the orientation of the determined CPO reference frame is highlighted.

we re-ran this simple shear path ($\sigma_{xz} \rightarrow \sigma_{yz}$) using two other methods for defining the CPO reference frame (SVD, and max(ODF), see in Supporting Information Text 1;Figure 6D). For this path, correcting the eigenvectors of the second-order orientation tensor for orthogonality using the singular value decomposition (SVD) method gives results that are closest to the VPSC simulations: strain rates calculated using both VPSC and the CPO2Hill v3 remain as low as, or lower than, the isotropic strain rates up to strain of 10. This suggests that, for this specific deformation path, the SVD-based CPO reference frame aligns the CPO best with the model frame, so that the orthotropic symmetry assumptions are most nearly satisfied.

Statistically, the best model is v3, which is closest to the VPSC results in all tests, including the test against laboratory data and the simple shear tests. CPO2Hill model v3 has the following relationship between the Hill coefficients and the eigenvalues of the mean orientation tensors of the olivine [100]-, [010]-, and [001]-axes (equations 16– 21):

$$\begin{aligned} F = {} & 0.592{a_1}^2 - 0.832a_1 - 0.001a_2 - \frac{0}{a_3} \\ & + 0.380{b_1}^2 - 0.533b_1 + 0.468b_2 - \frac{0.001}{b_3} \\ & - 1.249{c_1}^2 + 1.0750c_1 - 0.168c_2 + \frac{0.003}{c_3} + 0.52 \end{aligned} \tag{16}$$

$$\begin{aligned} G = {} & -1.695{a_1}^2 + 1.336a_1 - 0.1840a_2 + \frac{0}{a_3} \\ & + 0.750{b_1}^2 + 0.691b_1 + 0.377b_2 - \frac{0.002}{b_3} \\ & - 0.670{c_1}^2 - 0.552c_1 - 0.428c_2 + \frac{0.003}{c_3} + 0.26 \end{aligned} \tag{17}$$

$$\begin{aligned} H = {} & -1.140{a_1}^2 + 1.353a_1 + 0.751a_2 - \frac{0.002}{a_3} \\ & - 0.256{b_1}^2 - 1.006b_1 - 0.116b_2 + \frac{0.003}{b_3} \\ & + 0.684{c_1}^2 - 0.031c_1 - 0.080c_2 + \frac{0.006}{c_3} + 0.75 \end{aligned} \tag{18}$$

$$\begin{aligned} L = {} & -3.511{a_1}^2 + 2.686a_1 + 0.360a_2 - \frac{0.001}{a_3} \\ & + 3.948{b_1}^2 - 3.816b_1 - 0.779b_2 + \frac{0.004}{b_3} \\ & + 4.122{c_1}^2 - 2.483c_1 - 1.320c_2 + \frac{0.002}{c_3} + 2.00 \end{aligned} \tag{19}$$

$$\begin{aligned} M = {} & 4.537{a_1}^2 - 3.228a_1 + 0.276a_2 + \frac{0.007}{a_3} \\ & - 7.447{b_1}^2 + 5.7640b_1 - 1.4030b_2 + \frac{0.032}{b_3} \\ & + 2.968{c_1}^2 - 3.435c_1 - 2.266c_2 + \frac{0.122}{c_3} + 2.44 \end{aligned} \tag{20}$$

$$\begin{aligned} N = {} & 7.8730{a_1}^2 - 7.934a_1 - 2.588a_2 + \frac{0.030}{a_3} \\ & + 7.606{b_1}^2 - 5.469b_1 - 0.348b_2 + \frac{0.064}{b_3} \\ & - 1.788{c_1}^2 + 2.255c_1 + 3.023c_2 - \frac{0.103}{c_3} + 3.70 \end{aligned} \tag{21}$$

All other CPO2Hill model coefficients are available with the published data (*Kiraly et al.*, 2026).

4.1 Implementation in ASPECT

The aim behind developing the method of CPO2Hill was to integrate CPO induced anisotropic viscosity for olivine into large-scale geodynamic models. ASPECT, the Advanced Solver for Planetary Evolution, Convection, and Tectonics (*Bangerth et al.*, 2024) is a widely used code for regional and global geodynamic models. It allows for utilisation of particles-in-cell within adaptive mesh refinement (*Gassmöller et al.*, 2018), and includes a version of D-Rex for CPO tracking on advected particles (*Kaminski et al.*, 2004; *Fraters and Billen*, 2021). To test the usability of our method presented in this paper, we implemented a new material model in ASPECT that calculates anisotropic viscosity based on the texture that develops on particles using the D-Rex method. Based on the CPO implementation by *Fraters and Billen* (2021), the eigenvectors and eigenvalues of the second-order orientation tensor of the tracked CPO are calculated on the particles. The eigenvectors are used to construct the rotation matrix, R, which describes the CPO reference frame. For computational efficiency, this 3-by-3 rotation matrix is converted to euler angles ($\varphi_1, \theta, \varphi_2$) for storage and interpolation. Thus, the 3 times 3 eigenvalues and the 3 euler angles describing the orientation of the mean CPO reference frame are interpolated from the particles to the compositional fields. These values are then utilised in the material model, where the Hill coefficients are computed from the eigenvalues using the relationship in the best fit model CPO2Hill v3 (equation 16– 21). The Hill coefficients form the anisotropy tensor for fluidity in the CPO reference frame (A; equation 6), and influence the scalar fluidity, which we define as the non-tensorial part of the right-hand side of equation (5) (i.e. as $\frac{2}{3}\gamma_0 e^{(-Q/RT)}{\sigma_I}^{n-1}$). Since the determinant of the anisotropy tensor for fluidity is 0, it is a singular, non-invertible tensor. Its inverse, the anisotropy tensor for viscosity, is thus obtained using the Moore-Penrose inverse (pseudoinverse) method, which is implemented with singular value decomposition in the LAPACK linear algebra package (*Demmel*, 2003) that is included in the deal.ii library and thus in ASPECT. The scalar, but stress-dependent, component of anisotropic viscosity is computed following

equation (3) and equation (5). Since the anisotropic stress is also dependent on this scalar anisotropic viscosity, this mutual dependence might cause numerical instability. As a result, the scalar viscosity is damped with a fixed-point iteration, in which only half of the computed change is applied at each iteration until convergence is achieved. Finally, the anisotropy tensor for viscosity is rotated from the CPO reference frame into the model reference frame using the rank-4 version of the rotation matrix R, as defined by the mean CPO reference frame.

We test this new material model in ASPECT in a shear box, where we impose simple shear deformation in the *x*-direction normal to the *z*-plane. Using CPO2Hill model v3, we find that the modelled evolution of the anisotropic tensor for viscosity shows similar trends to the results computed in MATLAB (Figure S20), however some differences are present due to the different texture evolution models, which is expected based on comparisons of textures evolving in D-Rex vs in MDM (*Wang et al.*, 2024). In ASPECT, the effective viscosity drops below 50% of its initial value at an accumulated strain of 10. This weakening is less than what we observe directly in the CPO2Hill models, likely due to the damping we had to employ in the iterations to reach convergence. Time and memory usage in a shear box model with anisotropic viscosity, as compared to scalar isotropic viscosity, increase by factors of 2.7 and 12.3, respectively. The majority of the increase happens in procedures using the anisotropic tensor, for example, assembling and solving the Stokes equations, and interpolation from particles to fields. This drop in computational efficiency is thus within our expectations and not very expensive, since the tensor representation of viscosity uses 81 components compared to a single scalar in the isotropic case. In larger geodynamic models, this factor could be similar or lower, since anisotropic viscosity might not be enabled in the whole model domain.

5 Conclusions

We demonstrated that olivine CPO-related anisotropic viscosity can be characterised using a linear combination of parameters describing the CPO, based on the second-order mean orientation tensors. The magnitude of anisotropy predicted from the CPO2Hill models is comparable to laboratory experiments and previous models. This new method allows for an efficient way of deriving the full viscosity tensor for any given CPO, which can be used in combination with any texture evolution models for olivine, and can be used in advanced geodynamic codes, such as ASPECT. Based on the performance of ASPECT using CPO-related anisotropic viscosity within a simple shear experiment, we suggest that our approach has great potential as a modelling approach for incorporating 3D viscous anisotropy within complex geodynamic processes. Thus, we now have a new tool that will allow us to better explore the relationship between mantle flow, CPO and seismic anisotropy in complex areas such as around subduction zones (*Wang et al.*, 2024, 2025).

Acknowledgements

We thank our editor, Lukas Fuchs, and the two reviewers, Andrea Tommasi and Manuele Faccenda, for their constructive feedback on this work. This research was supported by the European Union (ERC, DYNAMICE, 101162078). Views and opinions expressed are, however, those of the author(s) only and do not necessarily reflect those of the European Union or the European Research Council. Neither the European Union nor the granting authority can be held responsible for them. The research was further supported by the Research Council of Norway's projects 314742 (ANIMA) and 332523 (Center for Planetary Habitability). We thank the Norwegian Research Infrastructure Service (NRIS/Sigma2) for providing the computational resources via project NN9894k. We also thank the Computational Infrastructure for Geodynamics, funded by the National Science Foundation under awards EAR-0949446 and EAR-1550901, for supporting the development of ASPECT.

Author contributions

Á.K. has developed the methodology, collected and analysed data, wrote the original manuscript and created the original figures. **Y.W.** contributed to data collection, numerical implementation, and wrote and edited the original manuscript. **C.P.C** has contributed to the method development and wrote and edited the original manuscript. **L.N.H.** has contributed to the method development, provided data from laboratory measurements, and edited the original manuscript. **B.M.** has contributed to the data analysis and method development and edited the original manuscript.

Data availability

Supporting Information is available with this paper. All additional data are published according the FAIR data sharing principles in \citep{Kiraly2026-bq}. VPSC simulations were done with VPSC 8, available on GitHub (https://github.com/lanl/VPSC_code.git). The cookbook to run ASPECT with CPO induced anisotropy can be downloaded from here: https://github.com/Wang-yijun/aspect/releases/tag/v2.0.

Competing interests

The authors declare that they have no competing interests.

Copyright notice

References

Bangerth, W., J. Dannberg, M. Fraters, R. Gassmoeller, A. Glerum, T. Heister, R. Myhill, and J. Naliboff (2024), ASPECT: Advanced solver for planetary evolution, convection, and tectonics, user manual, doi: http://-doi.org/10.6084/M9.FIGSHARE.4865333.V12.

Becker, T. W., and H. Kawakatsu (2011), On the role of anisotropic viscosity for plate-scale flow: ANISOTROPIC VISCOSITY, *Geophysical Research Letters*, *38*(17), 1–5, doi: http://-doi.org/10.1029/2011gl048584.

Bhatnagar, N. S., and R. P. Gupta (1967), On the constitutive equations of the orthotropic theory of creep, *Wood Science and Tech-*

nology, *1*(2), 142–148, doi: http://doi.org/10.1007/bf00353385.

Bingham, C. (1974), An antipodally symmetric distribution on the sphere, *Annals of Statistics*, *2*(6), 1201–1225, doi: http://-doi.org/10.1214/aos/1176342874.

Blackman, D. K., D. E. Boyce, O. Castelnau, P. R. Dawson, and G. Laske (2017), Effects of crystal preferred orientation on upper-mantle flow near plate boundaries: rheologic feedbacks and seismic anisotropy, *Geophysical Journal International*, *210*(3), 1481–1493, doi: http://doi.org/10.1093/gji/ggx251.

Christensen, U. R. (1987), Some geodynamical effects of anisotropic viscosity, *Geophysical Journal International*, *91*(3), 711–736, doi: http://doi.org/10.1111/j.1365-246x.1987.tb01666.x.

Christodoulou, N., and C. N. Tomé (2025), Anisotropy of plastic flow in Zr-2.5Nb pressure tube material analysed using a viscoplastic self-consistent approach, *Acta materialia*, *283*(120503), 120,503, doi: http://doi.org/10.1016/j.actamat.2024.120503.

de Oliveira, L. M. C. (2020), Intraplate strain localization due to olivine viscous anisotropy in the lithospheric mantle, Ph.D. thesis, Université Montpellier.

Demmel, J. (2003), LAPACK: a portable linear algebra library for supercomputers, in *IEEE Control Systems Society Workshop on Computer-Aided Control System Design*, pp. 1–7, IEEE, doi: http://doi.org/10.1109/cacsd.1989.69824.

Durham, W. B., and C. Goetze (1977), Plastic flow of oriented single crystals of olivine: 1. Mechanical data, *Journal of Geophysical Research*, *82*(36), 5737–5753, doi: http://-doi.org/10.1029/jb082i036p05737.

Fraters, M. R. T., and M. I. Billen (2021), On the implementation and usability of crystal preferred orientation evolution in geodynamic modeling, *Geochemistry, Geophysics, Geosystems: G(3)*, *22*(10), e2021GC009,846, doi: http://-doi.org/10.1029/2021gc009846.

Gassmöller, R., H. Lokavarapu, E. Heien, E. G. Puckett, and W. Bangerth (2018), Flexible and scalable particle-in-cell methods with adaptive mesh refinement for geodynamic computations, *Geochemistry, Geophysics, Geosystems: G(3)*, *19*(9), 3596–3604, doi: http://doi.org/10.1029/2018gc007508.

Han, D., and J. Wahr (1997), An analysis of anisotropic mantle viscosity, and its possible effects on post-glacial rebound, *Physics of the Earth and Planetary Interiors*, *102*(1-2), 33–50, doi: http://-doi.org/10.1016/s0031-9201(96)03268-2.

Hansen, L. N., M. E. Zimmerman, and D. L. Kohlstedt (2012), Laboratory measurements of the viscous anisotropy of olivine aggregates, *Nature*, *492*(7429), 415–418, doi: http://-doi.org/10.1038/nature11671.

Hansen, L. N., C. P. Conrad, Y. Boneh, P. Skemer, J. M. Warren, and D. L. Kohlstedt (2016a), Viscous anisotropy of textured olivine aggregates: 2. Micromechanical model, *Journal of Geophysical Research. Solid Earth*, *121*(10), 7137–7160, doi: http://-doi.org/10.1002/2016jb013240.

Hansen, L. N., J. M. Warren, M. E. Zimmerman, and D. L. Kohlstedt (2016b), Viscous anisotropy of textured olivine aggregates, Part 1: Measurement of the magnitude and evolution of anisotropy, *Earth and Planetary Science Letters*, *445*, 92–103, doi: http://-doi.org/10.1016/j.epsl.2016.04.008.

Hansen, L. N., M. Faccenda, and J. M. Warren (2021), A review of mechanisms generating seismic anisotropy in the upper mantle, *Physics of the Earth and Planetary Interiors*, *313*(106662), 106,662, doi: http://doi.org/10.1016/j.pepi.2021.106662.

Hill, R. (1948), A theory of the yielding and plastic flow of anisotropic metals, *Proceedings of the Royal Society of London*, *193*(1033), 281–297, doi: http://-doi.org/10.1098/rspa.1948.0045.

Kaminski, E., N. M. Ribe, and J. T. Browaeys (2004), D-Rex, a program for calculation of seismic anisotropy due to crystal lattice preferred orientation in the convective upper mantle, *Geophysical Journal International*, *158*(2), 744–752, doi: http://-doi.org/10.1111/j.1365-246x.2004.02308.x.

Kiraly, A., C. P. Conrad, and L. Hansen (2020), Evolving viscous anisotropy in the upper mantle and its geodynamic implications, *Earth and Space Science Open Archive*, doi: http://-doi.org/10.1002/essoar.10503040.1.

Kiraly, A., Y. Wang, C. Conrad, L. Hansen, and B. Mather (2026), Dataset for the paper titled 'CPO2Hill: A new model linking olivine texture parameters to anisotropic viscous behavior' by Király et al, doi: http://doi.org/10.5281/ZENODO.18611490.

Kohlstedt, D. L., and L. N. Hansen (2015), Constitutive equations, rheological behavior, and viscosity of rocks, in *Treatise on Geophysics*, vol. 2, pp. 441–472, Elsevier, doi: http://-doi.org/10.1016/b978-0-444-53802-4.00042-7.

Korenaga, J., and S.-I. Karato (2008), A new analysis of experimental data on olivine rheology, *Journal of Geophysical Research*, *113*(B2), 1–23, doi: http://doi.org/10.1029/2007jb005100.

Lebensohn, R. A., and C. N. Tomé (1993), A self-consistent anisotropic approach for the simulation of plastic deformation and texture development of polycrystals: Application to zirconium alloys, *Acta metallurgica et materialia*, *41*(9), 2611–2624, doi: http://doi.org/10.1016/0956-7151(93)90130-k.

Lev, E., and B. H. Hager (2008), Rayleigh-Taylor instabilities with anisotropic lithospheric viscosity, *Geophysical Journal International*, *173*(3), 806–814, doi: http://doi.org/10.1111/j.1365-246x.2008.03731.x.

Lev, E., and B. H. Hager (2011), Anisotropic viscosity changes subduction zone thermal structure: ANISOTROPIC VISCOSITY CHANGES WEDGE THERMAL STRUCTURE, *Geochemistry, Geophysics, Geosystems: G(3)*, *12*(4), doi: http://-doi.org/10.1029/2010gc003382.

Mainprice, D., F. Bachmann, R. Hielscher, and H. Schaeben (2015), Descriptive tools for the analysis of texture projects with large datasets usingMTEX: strength, symmetry and components, *Geological Society Special Publication*, *409*(1), 251–271, doi: http://doi.org/10.1144/sp409.8.

Mameri, L., A. Tommasi, J. Signorelli, and L. N. Hansen (2019), Predicting viscoplastic anisotropy in the upper mantle: a comparison between experiments and polycrystal plasticity models, *Physics of the Earth and Planetary Interiors*, *286*, 69–80, doi: http://doi.org/10.1016/j.pepi.2018.11.002.

Mameri, L., A. Tommasi, J. Signorelli, and R. Hassani (2020), Olivine-induced viscous anisotropy in fossil strike-slip mantle shear zones and associated strain localization in the crust, *Geophysical Journal International*, *224*(1), 608–625, doi: http://-doi.org/10.1093/gji/ggaa400.

Mameri, L., A. Tommasi, A. Vauchez, J. Signorelli, and R. Hassani (2023), Structural inheritance controlled by olivine viscous anisotropy in fossil mantle shear zones with different past kinematics, *Tectonophysics*, *863*(229982), 229,982, doi: http://-doi.org/10.1016/j.tecto.2023.229982.

Mühlhaus, H.-B., L. Moresi, B. Hobbs, and F. Dufour (2002), Large amplitude folding in finely layered viscoelastic rock structures, *Pure and Applied Geophysics*, *159*(10), 2311–2333, doi: http://-doi.org/10.1007/s00024-002-8737-4.

Mühlhaus, H.-B., M. Čada, and L. Moresi (2003), Anisotropic convection model for the earth's mantle, in *Lecture Notes in Computer Science*, *Lecture Notes in Computer Science*, vol. 2659, edited by P. M. A. Sloot, D. Abramson, A. V. Bogdanov, Y. E. Gorbachev, J. J. Dongarra, A. Y. Zomaya, G. Goos, J. Hartmanis, and J. van Leeuwen, pp. 788–797, Springer Berlin Heidelberg, Berlin, Heidelberg, doi: http://doi.org/10.1007/3-540-44863-2_77.

Rathmann, N. M., K. Mosegaard, I. M. O. Bekkevold, D. A. Lilien, and D. J. Prior (2024), A spectral directors method for modeling the coupled evolution of flow and CPO in polycrystalline Olivine, *Geochemistry, Geophysics, Geosystems: G(3)*, *25*(12), e2024GC011,831, doi: http://doi.org/10.1029/2024gc011831.

Sachs, G. (1928), Plasticity problems in metals, *Transactions of the Faraday Society*, *24*(0), 84, doi: http://-doi.org/10.1039/tf9282400084.

Signorelli, J., R. Hassani, A. Tommasi, and L. Mameri (2021), An effective parameterization of texture-induced viscous anisotropy in orthotropic materials with application for modeling geodynamical flows, *Journal of Theoretical, Computational and Applied Mechanics*, doi: http://doi.org/10.46298/jtcam.6737.

Skemer, P., I. Katayama, Z. Jiang, and S.-I. Karato (2005), The misorientation index: Development of a new method for calculating the strength of lattice-preferred orientation, *Tectonophysics*, *411*(1-4), 157–167, doi: http://-doi.org/10.1016/j.tecto.2005.08.023.

Taylor, G. I. (1938), Plastic Strain in Metals, *Journal of Inst. Met.*, *62*(307).

Vollmer, F. W. (1990), An application of eigenvalue methods to structural domain analysis, *Geological Society of America Bulletin*, *102*(6), 786–791, doi: http://doi.org/10.1130/0016-7606(1990)102<0786:aaoemt>2.3.co;2.

Wang, Y., Centre for Planetary Habitability (PHAB), University of Oslo, Oslo, Norway, A. Király, C. Conrad, L. Hansen, and M. Fraters (2024), The importance of anisotropic viscosity in numerical models, for Olivine textures in shear and subduction deformations, *Tektonika*, *2*(1), 157–173, doi: http://-doi.org/10.55575/tektonika2024.2.1.67.

Wang, Y., A. Király, C. P. Conrad, and V. Maupin (2025), Mantle flow and anisotropy in subduction zones: Modeling and clustering of Olivine textures, *Geochemistry, Geophysics, Geosystems: G(3)*, *26*(7), e2025GC012,160, doi: http://-doi.org/10.1029/2025gc012160.